Pergamon

0956-7151(94)E0032-C

Acta metall. mater. Vol. 42, No. 7, pp. 2233–2246, 1994

0956-7151/94 $7.00 + 0.00

A COUPLED FINITE ELEMENT–CELLULAR AUTOMATON MODEL FOR THE PREDICTION OF DENDRITIC GRAIN STRUCTURES IN SOLIDIFICATION PROCESSES

Ch.-A. GANDIN and M. RAPPAZ

Laboratoire de Métallurgie Physique, Ecole Polytechnique Fédérale de Lausanne, MX-G, CH-1015 Lausanne, Switzerland

(Received 29 September 1993; in revised form 10 January 1994)

Abstract—A new algorithm based upon a 2-dimensional Cellular Automaton (CA) technique is proposed for the simulation of dendritic grain formation during solidification. The CA model takes into account the heterogeneous nucleation, the growth kinetics and the preferential growth directions of the dendrites. This new CA algorithm, which applies to non-uniform temperature situations, is fully coupled to an enthalpy-based Finite Element (FE) heat flow calculation. At each time-step, the temperature at the cell locations is interpolated from those at the FE nodal points in order to calculate the nucleation-growth of grains. The latent heat released by the cells and calculated using a Scheil-type approximation is fed back into the FE nodal points. The coupled CA–FE model is applied to two solidification experiments, the Bridgman growth of an organic alloy and the one-dimensional solidification of an Al–7wt% Si alloy. In the first case, the predicted boundaries between grains are in good agreement with experiment, providing the CA cell size is of the order of the dendrite spacing. For the second experiment, the quality of the coupled CA–FE model is assessed based upon grain structures and cooling curves. The columnar-to-equiaxed transition and the occurrence of a recalescence are shown to be in good agreement with the model.

Résumé—Un nouvel algorithme d'Automate Cellulaire (AC) bi-dimensionnel est proposé pour simuler la formation de grains dendritiques lors de la solidification. Le modèle tient compte de la germination hétérogène, de la cinétique de croissance et des directions de croissance préférentielles des dendrites. L'algorithme, applicable à des situations de thermique non-uniforme, est couplé à des calculs d'éléments finis (EF) basés sur une méthode enthalpique. A chaque pas de temps, la température des cellules est interpolée à partir de celles des noeuds du maillage d'EF afin de calculer la germination-croissance des grains. La chaleur latente, libérée par les cellules et calculée à l'aide de l'approximation de Scheil, est rétrocédée aux noeuds du maillage d'EF. Le modèle AC–EF est appliqué au cas de deux expériences de solidification: la croissance dirigée dans un dispositif de type Bridgman d'un alliage organique et la solidification unidirectionnelle d'un alliage Al–Si7%pds. Dans le premier cas, les frontières prédites entre les grains présentent un bon accord avec l'expérience lorsque la taille des cellules approche l'espacement interdendritique. Pour la seconde expérience, la qualité des prédictions du modèle AC–EF est testée pour la structure des grains et les courbes de refroidissement. Il est montré que la transition colonnaire-équiaxe et l'existence d'une recalescence sont correctement prédites par le modèle.

Zusammenfassung—Ein neuer 2-dimensionaler Zellautomatenalgorithmus (ZA) wird vorgeschlagen, welcher die Entstehung dendtrischer Körner während der Estarrung zu simulieren erlaubt. Das Modell berücksichtigt die heterogene Keimbildung, die Wachstumskinetik und die bevorzugten Wachstumsrichtungen der Dendriten. Der Algorithmus, der auf thermisch ungleichförmige Problemstellungen angewandt werden kann, ist an eine auf der Enthalpie beruhenden Finite-Elemente-Methode (FE) gebunden. Bei jedem Zeitschritt wird die Zelltemperatur durch Interpolation der Temperaturen der Netzwerkknoten der FE bestimmt, um Keimbildung und Wachstum der Körner zu berechnen. Die von den Zellen freigesetzte latente Wärme, die mit einer Scheil-Näherung berechnet wird, diffundiert zu den Netzwerkknoten zurück. Das FE–ZA-Modell wird auf zwei Erstarrungsexperimente angewandt, die kontrollierte Erstarrung einer organischen Legierung in einem Bridgmanofen und die gerichtete Erstarrung einer Al–7gew% Si-Legierung. Im ersteren Fall stimmen die vorhergesagten Korngrenzen gut mit dem Experiment überein, wenn sich die Zellgrössen im Bereich der Dendritenabstände befinden. Im zweiten Fall dienen Kornstruktur und Abkühlkurven der Bewertung des FE–ZA Modells. Der experimentell beobachtete Übergang von säulenförmigem zu gleichachsigem Wachstum und das Auftreten einer Rekaleszenz werden von dem Modell gut reproduziert.

INTRODUCTION

Probabilistic models of solidification for the prediction of dendritic grain structures in solidification processes [1–6] have been developed recently by several authors. Adapting a Monte Carlo (MC) procedure previously developed by Anderson *et al.* [7] for recrystallisation and grain growth to the case of

solidification, Brown and Spittle [1, 2] and Ohsasa [3] have been able to compute micrographic cross sections in castings which reproduced the grain competition occurring in the columnar zone and the columnar-to-equiaxed transition (CET). Based upon a Potts model, such MC methods minimise an interfacial energy of unlike sites, i.e. of sites belonging to the solid–liquid interface for solidification or to the different grain boundaries for recrystallisation [8, 9]. However, they do not consider the specific aspects associated with dendritic solidification.

In cubic metals, it is well known that the selected grains in the columnar zone are those which have their ⟨100⟩ directions (i.e. the main growth direction of the dendrite trunks) most closely aligned with the heat flow direction [10, 11]. For this reason, the energy levels of the grains defined in the MC models should be variable and correlated with the growth anisotropy of the dendritic pattern within each grain. The "anisotropy intensity factor" introduced by Zhu and Smith [4, 5], in order to treat the competition of columnar grains, considers the growth rates of the grains in two directions, parallel and perpendicular to the heat flow direction. However, this parameter must be fitted to experimental results to obtain realistic grain structures and it does not relate to crystallographic orientations. Furthermore, no quantitative comparison with experimental observations has been made in order to estimate this parameter and to validate calculated grain boundaries.

Another drawback of the MC solidification models is that they do not explicitly integrate the growth kinetics of the solid–liquid interface, i.e. the relationship between the growth rate of the dendrite tips and their undercooling [12]. Furthermore, the correspondence between the MC time step used in the calculations and real time is not clear, since during each step N sites are randomly chosen among the N sites of the MC network (i.e. not all the sites located at the solid–liquid interface are investigated). To summarise, the grain growth mechanisms introduced in these solidification models are not physically sound. Similar limitations exist in the slightly different approach recently proposed by Yang *et al.* [6].

Based upon a Cellular Automaton (CA) technique, the approach developed by Rappaz and Gandin [13] for the prediction of the grain structure in castings specifically considers the crystallographic anisotropy of the grains and the growth kinetics of the dendrite tips. Assuming a given and uniform temperature field within the specimen, such model can predict quantitatively the effects of the cooling rate and solute concentration on the final grain structure. Charbon and Rappaz [14] have adopted a similar approach for the modelling of equiaxed grain structures in eutectic alloys. However, the major limitation of both the dendritic and eutectic models is the assumption of a uniform temperature situation (i.e. low Biot number). Rappaz *et al.* [15] have extended the probabilistic model of eutectic grain growth to a non-uniform temperature field by imposing a constant thermal gradient and cooling rate and neglecting the latent heat released by the grains.

The aim of the present contribution is to present a new approach which couples a finite element (FE) heat flow calculation with a 2-dimensional cellular automaton model (CA) describing the formation of grains in castings. For this end, the nucleation and growth algorithms previously described in Ref. [13] are adapted to non-uniform temperature situations and the latent heat liberated by the grains, more precisely by the cells belonging to the grains, is fed back into the macroscopic model. Prior to applying such a CA–FE model to the study of the CET occurring in a one-dimensional aluminium–silicon alloy, the grain competition which has been observed in an organic alloy by Esaka [16, 17] is used to support the CA growth algorithm.

EXPERIMENTAL

Grain selection in the columnar zone

As shown by Esaka [16, 17], *in situ* observations of the dendritic solidification of transparent organic analogues is a very powerful tool for the study of the selection occurring among the grains in the columnar zone. Because solidification occurs between two glass sheets whose separation is small, only one dendrite layer grows in the thickness of the solidifying volume and can be easily observed. This point is of great importance if a comparative analysis is to be done with a two-dimensional model of grain structure formation.

The three video sequences of Fig. 1 show the selection of columnar grains in an organic binary alloy solidified under one-dimensional Bridgman conditions as observed under a microscope by Esaka [17]. The first sequence at the bottom has been isolated from the latter development stage of the microstructure in order to visualise the dendrite tip position during growth, whereas the two subsequent video sequences have been assembled to clearly reveal the grain boundaries. As can be seen from the ⟨100⟩ dendrite trunk orientations, three grains are present at the beginning (bottom of Fig. 1): the two external grains have their ⟨100⟩ preferential growth direction almost perpendicular to the horizontal isotherms whereas the grain in the centre has its ⟨100⟩ crystallographic orientation at about 30° from the temperature gradient (vertical direction).

It is interesting to observe that for a constant thermal gradient and velocity of the liquidus isotherm, the two grain boundaries in Fig. 1 are straight lines. For the two grains on the left of Fig. 1 which have converging ⟨100⟩ dendrite trunk directions, the grain boundary coincides with the dendrite trunk of the left-hand grain for which the ⟨100⟩ crystallographic direction is almost aligned with the temperature gradient. This observation can be easily

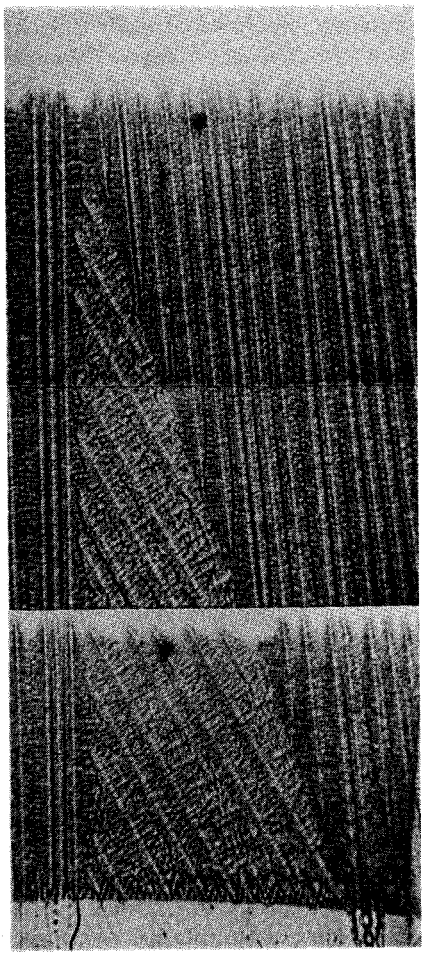

Fig. 1. Competition between three columnar grains of a succinonitrile–1.3wt% acetone alloy solidified under a constant thermal gradient, $G = 1900$ K/m, and a velocity of the liquidus isotherm, $v_L = 86 \cdot 10^{-6}$ m/s (picture assembled from three sequences of the video tape recorded by Esaka [16]).

explained: for a given velocity of the liquidus isotherm, v_L, dendrites having a misorientation, θ, with respect to the temperature gradient grow with a higher velocity, $v_\theta = v_L/\cos(\theta)$, in order to keep stationary growth conditions. Since the growth rate of the dendrite tips is an increasing function of the undercooling [12], the dendrite tips of the misaligned central grain in Fig. 1 have a higher growth rate and thus a higher undercooling. In a given temperature gradient, this means that they lie slightly behind the dendrite tips of the well-aligned grain at left of Fig. 1 and that their growth is stopped by the solute field of the secondary arms of these well-aligned dendrites.

For two neighbouring grains having ⟨100⟩ diverging orientations (the situation at the right of Fig. 1), an open region of liquid continuously forms in-between the dendrite trunks. Secondary arms can therefore grow in this region and, by branching mechanisms of tertiary arms, lead to the formation of new primary dendrite trunks. As can be seen in Fig. 1, new trunks form on the sides of both grains but with quite different spacings. It appears that the primary spacing of the central grain, λ_{1c}, is larger than that of the right-hand grain, λ_{1r}. This result does not follow the $G^{-1/2} \cdot v^{-1/4}$ dependence predicted by simple models [18] since, for a fixed temperature gradient, G, the velocity, v, of the dendrites within the central grain is larger than that of the dendrites in the right-hand grain. The same result was discovered by Grugel and Zhou [19].

In Fig. 1 it also appears that the variations of primary trunk spacing within each grain are directly associated with the chaotic behaviour of the branching mechanisms at grain boundaries (growth competition between secondary and tertiary arms of the two grains [17]). Nevertheless, new trunks within each grain form at the grain boundaries with average spatial frequencies, f_c and f_r. The angle, θ_B, of the grain boundary with respect to the temperature gradient can thus be calculated using these average values

$$\sin(\theta_c - \theta_B) = \lambda_{1c} \cdot f_c \quad \text{and} \quad \sin(\theta_B - \theta_r) = \lambda_{1r} \cdot f_r \quad (1)$$

where θ_c and θ_r are the angles characterising the dendrite trunk directions for the central and right-hand side grains, respectively. If f_{cr} is the ratio of the two frequencies (i.e. the ratio at which new trunks appear at the grain boundary, $f_{cr} = f_c/f_r$), then

$$\tan \theta_B = \frac{\frac{\lambda_{1c}}{\lambda_{1r}} \cdot f_{cr} \cdot \sin \theta_r + \sin \theta_c}{\frac{\lambda_{1c}}{\lambda_{1r}} \cdot f_{cr} \cdot \cos \theta_r + \cos \theta_c}. \quad (2)$$

Considering that four new dendritic trunks appear in Fig. 1 in the central grain while ten form in the right-hand grain (i.e. $f_{cr} = 4 \div 10$), the application of equation (2) to this case ($\theta_c = 30°$, $\theta_r = 11°$, $\lambda_{1c} = 310\ \mu$m and $\lambda_{1r} = 177\ \mu$m) leads to a value of θ_B equal to 22°. This value is to be compared with the experimentally observed grain boundary angle $\theta_B = 19°$. It must be emphasised that equation (2) is only a geometrical relationship deduced from experimental observation. It cannot be used as a predictive tool to calculate the boundary between two grains of diverging orientations since neither the primary trunk spacings nor the frequency of the appearance of these trunks at the boundary can be estimated from simple analytical models.

In summary, the growth of a single grain can be seen as the development of a single dendritic network with given ⟨100⟩ directions corresponding to primary, secondary and tertiary arms. Neglecting the "incubation time" which is necessary for a secondary or tertiary dendrite arm to escape from its neighbours and to become a free growing dendrite tip, each part of this dendritic network develops with the same growth kinetics law relating the local growth rate to the local undercooling. In a uniform temperature gradient, the resulting shape of the grain will be a square [13] but in a given temperature gradient,

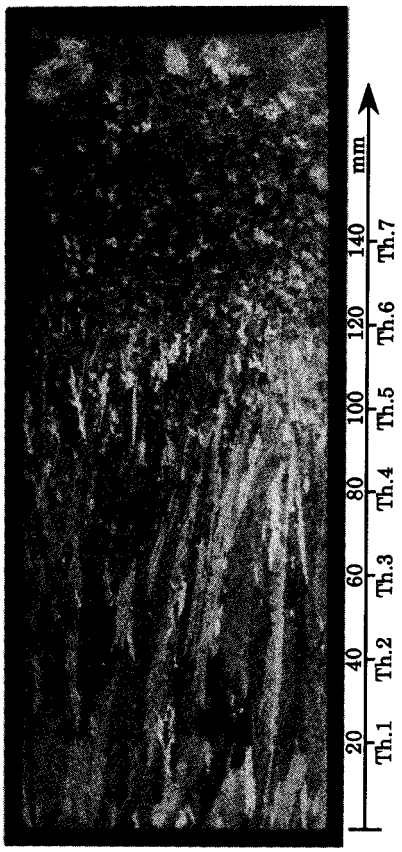

Fig. 2. Grain structure in a longitudinal section of a Al–7wt% Si alloy cylinder unidirectionally solidified over a copper chill plate.

the local undercooling, and thus the local growth rate, varies. Accordingly, in a Bridgman-type experiment such as that used for the solidification of organic analogues (Fig. 1), the secondary and tertiary arms which are further away from the liquidus isotherm grow faster and determine the competition which occurs at the boundaries of two grains having diverging ⟨100⟩ orientations. The crystallographic orientations of the grains being defined, the grain selection then appears as a fully deterministic process which is only governed by the local solidification conditions and by the growth kinetics law of the alloy.

Columnar-to-equiaxed transition

The Al–7wt% Si ingot shown in Fig. 2 was solidified under well-controlled unidirectional solidification conditions using the experimental arrangement described by Ampuero *et al.* [20, 21]. In order to eliminate any convection associated with pouring, the liquid metal and mould were initially maintained at a constant temperature (superheat of 139°C). The temperature difference between the seven Pt–Pt10%Rh thermocouples (see locations in Fig. 2) was lower than 1°C before a water-cooled copper chill was applied to the bottom of the mould. In order to obtain one-dimensional cooling conditions, the lateral walls and top of the mould were made out of a highly insulating material (Promat™) whereas the bottom part was a thin plate of aluminium nitride having a large thermal conductivity. The heat flow leaving the ingot during solidification was determined by an inverse method calculation of the temperatures measured at precise locations in the copper chill [22]. It should also be pointed out that natural and solute convection is minimised with this experimental configuration using this alloy.

As is well known in dendritic solidification [10, 11, 18], the structure of conventionally cast ingots often consists of three distinct zones which can be clearly seen in Fig. 2: fine grains (outer equiaxed region) near the bottom mould surface, long columnar grains whose growth starts from the outer equiaxed region and finally an equiaxed region in the upper part of the casting. The transition from the columnar to the equiaxed zones (CET) has been the subject of many investigations. Winegard and Chalmers [23] first proposed that the dendritic equiaxed zone is a result of heterogeneous nucleation of grains in a large constitutionally undercooled region. But their theory was unable to explain the effect of the pouring temperature on the final grain size and the percentage of columnar and equiaxed zones. For that reason, Chalmers [24] proposed that, for a low pouring superheat, new crystals may rapidly form near the mould wall and move in the bulk of the liquid by convection motion. This so-called "big bang" nucleation theory and heterogeneous nucleation in the bulk can explain many of the solidification grain structures. Another factor intervening in the formation of equiaxed grains is the mechanical breaking [25] and remelting [26] of dendrite arms by convection. Finally, Southin [27] has shown that grains may also form at the top surface of an ingot which is open to atmosphere, thus defining a "fourth" zone in castings. If convection exists, these latter grains may be drawn into the liquid and contribute to the equiaxed region.

With the present experiment approximating convection-free one-dimensional heat flow conditions† most of the mechanisms of equiaxed grain formation mentioned before can be legitimately ruled out, in particular those proposed by Johnston *et al.* [25] and Jackson *et al.* [26]. Additionally, starting with a liquid metal which is insulated from the atmosphere by a closed mould having the same initial temperature, the "fourth" zone of castings [27] and the big bang nucleation [24] are also eliminated. Therefore, this leaves the heterogeneous nucleation in an undercooled liquid ahead of the growing columnar front

†The only fluid motion which can occur in this experiment is that associated with shrinkage and with the Marangoni effect. The first contribution produces a small fluid motion opposed to the displacement of the isotherms whereas the surface-driven flow is negligible considering the very small lateral thermal gradient at the free surface.

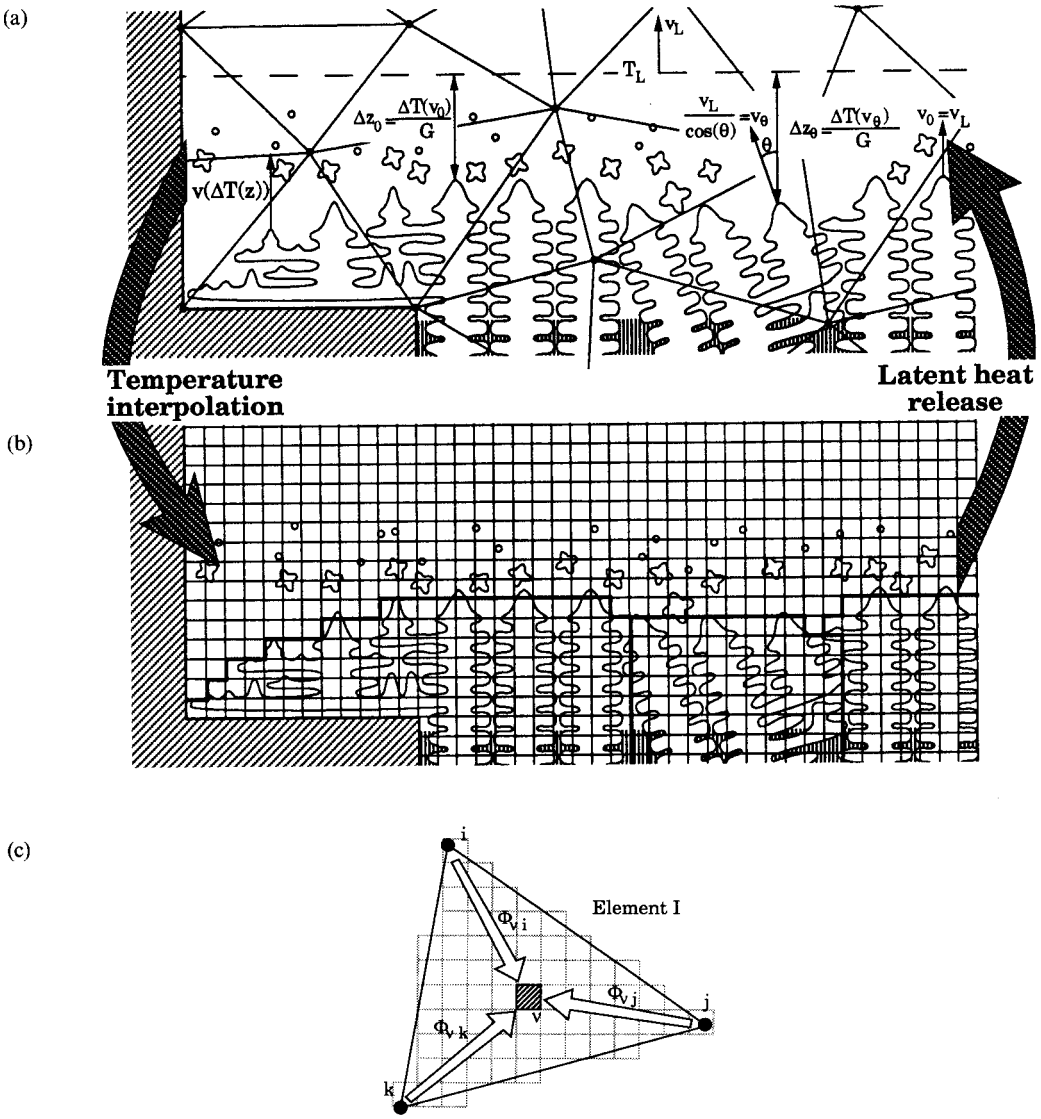

Fig. 3. Schematic diagram of a directional solidification experiment showing the competition among columnar grains, the heterogeneous nucleation and growth of equiaxed grains ahead of the columnar grains and the extension of a dendritic grain after passing a re-entrant corner of the mould. A typical triangular (FE) mesh (a) and the regular network of cells used in the CA model (b) are also shown together with the boundaries of the columnar grains (heavy lines in b) which would result from the CA–FE calculations. The three interpolation factors, ϕ_{vi}, ϕ_{vj}, ϕ_{vk}, from FE nodes i, j, k to CA cell v are schematically described as arrows in (c).

[23] as the only possible mechanism for the CET seen in Fig. 2.

Finally, the well-controlled solidification conditions achieved with the experimental arrangement described above allows the results to be used with a high degree of accuracy for validating the ability of the model to simulate both grain growth formation and the cooling curves.

MODEL

Introduction

Figure 3(a) summarises the situation already described in the previous section for the formation of dendritic grains in a small region of a casting of non-uniform cross-section (presence of a re-entrant corner). If the liquidus isotherm, T_L, moves in a thermal gradient, G, at a velocity, v_L, the undercooled region ahead of the well-aligned columnar dendrite tips, Δz_0, is given by the undercooling, $\Delta T_0 = \Delta T(v_L)$, divided by G. As explained above, the dendrite tip velocity, v_θ, of the misaligned grain at the centre is larger and so are the undercooling, $\Delta T_\theta = \Delta T(v_\theta)$, and the undercooled region, Δz_θ. Since an undercooled region of liquid is available between the liquidus isotherm and the dendrite tips, equiaxed grains can nucleate in this region [23, 28]. Additionally, dendrite arms can extend in open regions of

liquid such as that near to the re-entrant corner on the left of Fig. 3(a) or in-between two grains of diverging ⟨100⟩ orientations.

A finite element (FE) enmeshment which can be used for a heat flow calculation in the casting [Fig. 3(a)] and whose typical size is well adapted to the temperature gradients (i.e. macroscopic scale) is drawn superimposed to the schematic dendritic network. A regular network of square cells with a much finer scale (typically of the order of the secondary dendrite arm spacing) has been drawn in Fig. 3(b) for the modelling of the grain structure formation with the cellular automaton (CA) [13]. The aim of this is to combine the FE and CA calculations in a single model in order to predict simultaneously the microstructure development as a function of the thermal field and the influence of the latent heat release of the grains on the calculated thermal history (e.g. local undercooling, recalescence). For this purpose, interpolation coefficients are defined between nodal points of the FE mesh and CA cells as illustrated in Fig. 3(c). The CA cell, v, with its centre in the finite element I, has non-zero interpolation coefficients, ϕ_{vi}, ϕ_{vj}, and ϕ_{vk} with the FE nodes i, j, k, respectively.† As explained in more detail below, these interpolation coefficients allow the determination of the temperature at the cell locations using those known at the FE nodal points [LHS arrow in Fig. 3(a, b)]. The same coefficients are used to sum up, at the nodal points, the latent heat released by nucleation, growth and the thickening of the dendritic microstructure as calculated at the scale of the CA cells [RHS arrow in Fig. 3(a, b)].

Nucleation

As explained in Refs [13] and [29], heterogeneous nucleation occurring in the bulk liquid and at the surface of the casting is described by two distributions of nucleation sites which become active as undercooling increases. In the present case, Gaussian distributions have been used and thus the density of grains, n_v (n_s), formed at any undercooling, ΔT, in the bulk (surface) of the casting is given by

$$n_{v(s)}(\Delta T) = \int_0^{\Delta T} \left[\frac{\mathrm{d}n}{\mathrm{d}(\Delta T')}\right]_{v(s)} \cdot \mathrm{d}(\Delta T') \qquad (3)$$

where the entity in between the square brackets is the corresponding Gaussian nucleation site distribution.

Modelling of heterogeneous nucleation with the CA is straightforward. For the bulk of the liquid (i.e. for cells which do not touch the surface of the casting), undercoolings randomly generated with a Gaussian distribution are attributed to randomly chosen cells. The corresponding undercoolings, $\Delta T_v^{\mathrm{nuc}}$, of these predetermined "nucleation" cells are stored. (Another Gaussian distribution is used for the cells belonging to the boundary of the domain.) If a cell is chosen several times (i.e. if it contains more than one nucleation site), only the smaller nucleation undercooling is used. If, during a time-step, the local undercooling, ΔT_v^t, of a particular "nucleation" cell, v, which was still liquid becomes larger than the prescribed nucleation undercooling, $\Delta T_v^{\mathrm{nuc}}$, a new grain forms. As described in Ref. [13], the state index of this cell, which was zero when it was liquid, is then set to a positive integer value randomly chosen among a certain number of orientation classes. In two dimensions, the $]-45°, +45°]$ possible orientations of the four-fold symmetry dendrites was divided into 48 classes, thus resulting in orientation classes of less than 2 degrees of difference.

Growth algorithm

Studying the two-dimensional growth of equiaxed cyclohexanol crystals in a uniform thermal field, Ovsienko *et al.* [30] observed that the envelope outlining the dendrite tip positions was nearly square. The growth algorithm which was embedded in the CA model previously developed for uniform temperature specimens [13] was based on such observations. It was shown that a dendrite tip correction had to be introduced in order to retain the original misorientation of the parent nucleus. The capture of neighbouring cells by the growing dendritic network was then almost equivalent to the overall growth of a square envelope. Since this algorithm cannot be easily adapted to non-uniform temperature situations, a new procedure is reported here which describes the two-dimensional growth of a randomly oriented grain in any thermal field.

Let consider first a "nucleation" cell, v, for which the formation of a new grain had occurred at a time t_n (see Fig. 4). The main [10] and [01] crystallographic

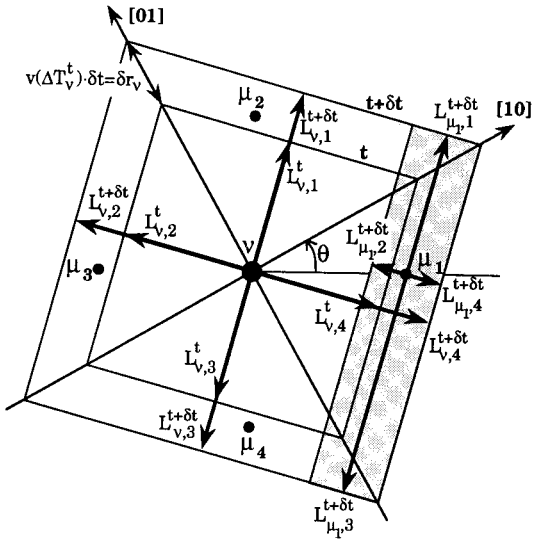

Fig. 4. Schematic diagram illustrating the growth algorithm used in the CA model for a dendritic grain whose [10] direction is misoriented by an angle θ with respect to the horizontal axis of the CA network.

†Greek, upper- and lower-case indices are used for the numbering of cells, elements and nodal points, respectively.

directions make an angle θ, respectively $\theta + \pi/2$, with respect to the horizontal axis. This "nucleation" cell, whose temperature is assumed to be locally uniform, is surrounded by four nearest-neighbour cells labelled μ_1, μ_2, μ_3 and μ_4. Neglecting the incubation time necessary for a spherical nucleus to become unstable and dendritic, it is assumed that the dendritic network within cell v develops as a square envelope. The four half-diagonals ($j = 1, 4$) of this square correspond to the dendrite tips directions and their extension, $^*L^t_{v,j}$, is therefore given by

$$^*L^t_{v,j} = \int_{t_n}^{t} v(\Delta T^{t'}_v) \cdot dt' \tag{4}$$

where $v(\Delta T^t_v)$ is the growth kinetics of the dendrite tip, as deduced from the model of Kurz *et al.* [12], the thermal history, T^t_v, at that cell location being given by the temperature field calculation. The growth of the $\langle 11 \rangle$ planes can also be monitored. Their position, $L^t_{v,j}$, from the centre of the cell, v, is given by

$$L^t_{v,j} = \frac{^*L^t_{v,j}}{\sqrt{2}} = \frac{1}{\sqrt{2}} \int_{t_n}^{t} v(\Delta T^{t'}_v) \cdot dt'. \tag{5}$$

At a critical time, t_c, the square will catch the four cell centres, μ_i. This will occur when

$$L^{t_c}_{v,j} = \frac{l}{\sqrt{2}} \cdot [\cos\theta + |\sin\theta|] \tag{6}$$

where l is the spacing between the cells. At that time, the four neighbouring cells will have their state index number set to the same value as that of the parent cell v, providing they are still liquid. Allowing other squares to grow within each of the cell $\mu_1 - \mu_4$ with the corresponding temperature at each cell location definitely biases the original misorientation of the grain, as shown in Ref. [13]. In order to remove this problem, rectangles are grown from each μ_i centre as shown in Fig. 4. The four $\langle 11 \rangle$ directions ($j = 1, 4$) at each cell centre, μ_i ($i = 1, 4$), grow with the same growth kinetics, $v(\Delta T^t_{\mu_i})/\sqrt{2}$, defined in equation (5) but with the local undercooling corresponding to each cell location. At the time of capture, t_c, these rectangles degenerate into segments whose size corresponds to the actual extension of the dendritic front which captured these sites. In Fig. 4, for example, the initial extension of the four $\langle 11 \rangle$ directions at site μ_1 will be such that: $L^0_{\mu_{1,1}} + L^0_{\mu_{1,3}} = \sqrt{2} \cdot l \cdot [\cos\theta + |\sin\theta|]$ and $L^0_{\mu_{1,2}} = L^0_{\mu_{1,4}} = 0$. In the time-stepping calculation, each of these extensions of the rectangle are updated as follows

$$L^t_{\mu_{i,j}} = L^0_{\mu_{i,j}} + \frac{1}{\sqrt{2}} \int_{t_c}^{t} v(\Delta T^{t'}_{\mu_i}) \cdot dt'$$

$$\cong L^{t-\delta t}_{\mu_{i,j}} + \frac{v(\Delta T^{t-\delta t}_{\mu_i}) \cdot \delta t}{\sqrt{2}} \quad (i, j) = 1, 4. \tag{7}$$

It should be pointed out that, in order to speed up the computations, the velocity, $v(\Delta T^t_{\mu_i})$, is computed as a function of the undercooling, $\Delta T^t_{\mu_i}$, at the cell centre and not at the four rectangle tips. This difference might become important if the temperature difference between two neighbouring cells, $G \cdot l$, becomes large compared to the local undercooling. It will be shown in the following section that an accurate prediction of the boundary between two columnar grains requires a sufficiently small cell spacing.

It is clear that the same growth algorithm can be applied to the "nucleation" cell (a square is a particular case of a rectangle) and to the capture of the four neighbours of each cell, μ_i (capture of four neighbours by a growing rectangle instead of a square). When a growing cell has all its neighbours with a non-zero index number, its $\langle 11 \rangle$ directions are no longer incremented. Finally, the time step, δt, used in the CA model must be such that: $v(\Delta T^t) \cdot \delta t < l$, i.e. the growth of the dendritic network during one time-step cannot exceed the cell spacing.

Coupling the FE and CA models

A linearised implicit FE enthalpy formulation of the heat flow equation can be written as [29, 31, 32]

$$\left[\frac{1}{\delta t} \cdot [M] + [K]^t \cdot \left[\frac{\partial T}{\partial H}\right]^t\right] \cdot \{\delta H\} = -[K]^t \cdot \{T\}^t + \{b\}^t \tag{8}$$

$[M]$ and $[K]^t$ are the mass and conductivity matrices, respectively, $\{b\}^t$, $\{T\}^t$ and $\{\delta H\}$ are the vectors corresponding to the boundary conditions, the temperatures and enthalpy variations at the nodes of the FE mesh, respectively. (The symbol "δH" has been preferred to "ΔH" in order to avoid confusion with any departure from equilibrium such as the undercooling ΔT.) The implicit equations have been linearised thus introducing the diagonal matrix $[\partial T/\partial H]^t$ containing the derivatives of the temperature over the enthalpy at the nodes. In order to remove oscillations which might occur at a eutectic plateau or near the liquidus of the alloy, this matrix can be replaced by $(\rho \cdot c_p)^{-1} \cdot [I]$ where $\rho \cdot c_p$ is the volumetric specific heat and $[I]$ is the identity matrix [31]. The resolution of equation (8) thus gives the enthalpy variations, δH_n, at the nodes during a time step, δt. As in the micro-macroscopic models of solidification [29, 32], these variations of enthalpy are then converted into variations of temperature and of volume fraction of solid using nucleation-growth models. In the present case, this conversion is carried out using the CA model as follows.

Within each time step, the known temperature at time t, T^t_v, and the volumetric enthalpy variation, δH_v, of the cell v are first interpolated by using the linear interpolation coefficients ϕ_{vn}

$$T^t_v = \sum_n \phi_{vn} \cdot T^t_n \tag{9}$$

$$\delta H_v = \sum_n \phi_{vn} \cdot \delta H_n \tag{10}$$

where the summation over the index (n) is carried out over all the nodal points of the finite element (I) which contains the cell (v) [e.g. three nodal points for a linear triangular element, see Fig. 3(c)]. For each cell, the unknown temperature, $T_v^{t+\delta t}$, and internal volume fraction of solid, $f_{s,v}^{t+\delta t}$ must satisfy the following relationship

$$\begin{aligned}\delta H_v &= \rho \cdot c_p \cdot \delta T_v - \Delta H_f \cdot \delta f_{s,v} \\ &= \rho \cdot c_p \cdot [T_v^{t+\delta t} - T_v^t] - \Delta H_f \cdot [f_{s,v}^{t+\delta t} - f_{s,v}^t]\end{aligned} \tag{11}$$

where ΔH_f is the latent heat of fusion per unit volume.

Three cases can be encountered for any cell:

(i) No variation of the volume fraction of solid

The explicit temperature, T_v^t, is above the liquidus of the alloy (or below the final eutectic temperature) in which case the volume fraction of solid of the cell does not evolve during the time step (i.e. $\delta f_{s,v} = 0$),

(ii) Solidification of an already mushy cell

The cell has an index $\neq 0$ and $T_L > T_v^t > T_{eut}$, i.e. it has nucleated or it has been captured by a growing grain but it is not fully solid. In this case, the volume fraction of solid in the cell is assumed to follow the microsegregation model of Scheil [18] (i.e. complete mixing of solute within the remaining liquid in the cell and no diffusion in the solid). Deriving the Scheil equation simply gives

$$\delta f_{s,v} = \frac{-\delta H_v}{\rho \cdot c_p \cdot (T_L - T_m) \cdot (k-1) \cdot [1 - f_{s,v}^t]^{(k-2)} + \Delta H_f} \tag{12}$$

where T_L and T_m are the liquidus and melting point of the alloy, respectively, and k is the partition coefficient.

If the cell temperature is equal to the eutectic temperature, T_{eut}, with a solid fraction lower than unity, $f_{s,v}^t < 1$, a simple isothermal transformation is made according to equation (11) until $f_{s,v}^t = 1$.

(iii) Capture or nucleation of a cell which was liquid

The cell has its index changed from zero to a positive integer number during the time step, δt. For a "nucleation cell" which was still liquid, this can occur if the local undercooling given by $(T_L - T_v^t)$ is larger than the prescribed nucleation undercooling, ΔT_v^{nuc} (see the "Nucleation" section). This also happens when the cell is captured by a growing grain (see the "Growth algorithm" section). In both cases, the whole cell is attributed a volume fraction of solid given by the Scheil model at the corresponding explicit temperature, T_v^t, i.e.

$$\delta f_{s,v} = 1 - \left[\frac{T_v^t - T_m}{T_L - T_m}\right]^{1/(k-1)}. \tag{13}$$

[Please note that equation (13) for a cell is roughly equivalent to the model of Flood and Hunt [33] which assumed a truncated Scheil equation for the modelling of the growth of a columnar front.]

It should be pointed out that the growth of a cell which has at least one liquid neighbour at time t is updated according to the procedure described previously, using the explicit dendrite tip velocity, $v(\Delta T_v^t)$.

The latent heat contributions of all the cells associated with points (i–iii) above are then fed back into the nodal points of the FE mesh according to

$$\delta f_{s,n} = \frac{\sum_v \phi_{vn} \cdot \delta f_{s,v}}{\sum_v \phi_{vn}} \tag{14}$$

where the summation is now carried out over all the cells belonging to the elements which have the nodal point, n, as a vertex (i.e. for which $\phi_{vn} \neq 0$). The denominator appearing in equation (14) is a normalisation factor.†

Once the $\delta f_{s,n}$ are known, the new temperatures at the nodal points can be calculated according to

$$\begin{aligned}\delta H_n &= \rho \cdot c_p \cdot \delta T_n - \Delta H_f \cdot \delta f_{s,n} \\ &= \rho \cdot c_p \cdot [T_n^{t+\delta t} - T_n^t] - \Delta H_f \cdot [f_{s,n}^{t+\delta t} - f_{s,n}^t]\end{aligned} \tag{15}$$

and the next FE heat flow calculation can be carried out using these updated temperatures. It should be emphasised that the time step used at the macro level is not necessarily equal to the time step used to calculate the nucleation-growth at the CA level. If required, the time step used to calculate the microstructure formation can be refined to meet the condition mentioned at the end of the "Growth algorithm" section. The scheme proposed here is therefore almost identical to the micro-enthalpy scheme proposed previously by Thévoz *et al.* [31, 32] for the deterministic calculation of the grain formation.

Test

The results shown in Fig. 5 have been calculated for a single grain using the growth algorithm described previously for a Moore configuration of the CA network [34] (i.e. the same growth algorithm was applied to the first- and second nearest neighbours of each cell). The growth kinetics of the dendrite tips, $v(\Delta T)$, was deduced from the experimental measurements of Esaka [16] for the succinonitrile–1.3wt%acetone alloy. It was fitted with a third order polynomial, the parameters of which are listed in Table 1. A linear temperature field, $T(x, y, t)$, was imposed at the FE nodes in order to validate the growth algorithm and no latent heat was released [i.e. only the coupling represented by the LHS arrow of Fig. 3 was used via the temperature interpolation of equation (9)]. Assuming that the nucleation

†The normalisation factor appearing in the denominator of equation (14) is almost equal to the diagonal coefficient of the lumped mass matrix, M_{nn}, divided by the volume of a cell.

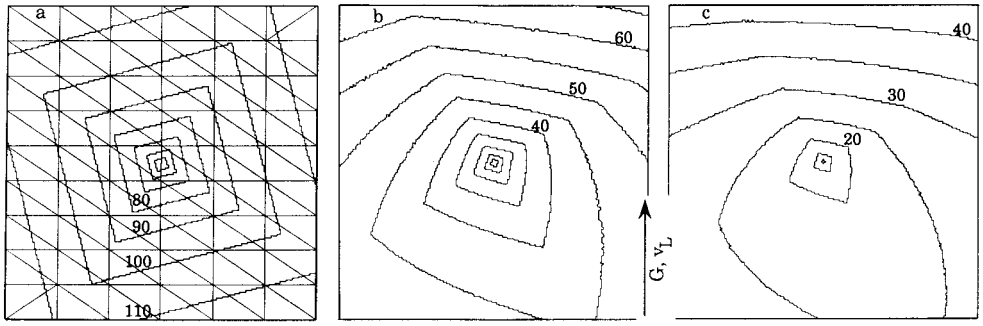

Fig. 5. Application of the grain growth algorithm for a single equiaxed grain solidifying in a uniform temperature field ($G = 0$ K/m) at a constant cooling rate ($\dot{T} = -0.01$ K/s) (a). The grain has been nucleated at the liquidus temperature and with $\theta = -30°$. The positions of the grain interface at the times indicated in the figures (in sec) have also been calculated in (b) and (c) for a given velocity of the liquidus isotherm, $v_L = 10^{-4}$ m/s, and two different thermal gradient, $G = 250$ and 500 K/m, respectively.

undercooling, ΔT_v^{nuc}, was equal to zero for a single cell at the centre of the CA network, a grain was nucleated with a misorientation $\theta = -30°$ with respect to the horizontal axis (see Fig. 4).

Figure 5(a) presents first the application of the growth algorithm to a uniform temperature situation imposed at the FE nodes. A grid of 200 × 200 cells (not shown) was superimposed to the FE mesh with triangular elements as shown in the figure. The thermal gradient, G, was zero and the cooling rate, $\dot{T}$, was imposed to -0.01 K/s at all the FE nodes. Superimposed onto the FE mesh are the calculated positions of the dendritic grain envelope as predicted by the CA model for the corresponding times labelled in this figure (in seconds unit). As the undercooling increases linearly with time, the growth rate of the dendrite arms envelope increases as the cubic power of time (see Table 1). As can be seen, the new growth algorithm proposed above does produce a square shape dendritic grain when applied to a uniform temperature situation, regardless of the grain misorientation with respect to the CA axes. As for the "dendrite tip" correction proposed in Ref. [13] for a uniform temperature field, this new algorithm retains the initial misorientation of the nucleus. However, it has the advantage of also handling non-uniform temperature situations as shown below.

Figures 5(b) and (c) show the results predicted by the CA–FE model when the same grain shown in Fig. 5(a) is placed in a non-uniform temperature situation. In both figures, the uniform thermal gradient, G, is vertical and the cooling rate, $\dot{T}$, is constant (the values are listed in the figure caption). As can be seen, the envelope of the grain extends faster towards the bottom of the domain because it is more undercooled as was already shown to be the case for eutectic grains [15]. The upper portion of the dendrites envelope tends to follow the horizontal liquidus isotherm, which moves upwards with a velocity $|v_L| = |\dot{T}| \cdot G^{-1}$. The stationary growth of the upper part of the grain envelope is characterised by a constant undercooling, ΔT_θ, with a value associated with the growth kinetics of the dendrites tips when $v = v_L/\cos\theta$ [i.e. $\Delta T_\theta = \Delta T(v_L/\cos\theta)$]. As could be expected, the adaptation of the grain envelope to the stationary situation is faster as the thermal gradient increases for a given velocity of the isotherm.

Although such results seem to be in qualitative agreement with the desired evolution of the grain envelope, further validation by experimentation is necessary, as is demonstrated in the next section.

RESULTS AND DISCUSSION

Grain selection in the columnar zone

A comparison with experimental observations of grain selection in organic analogues is first presented in Fig. 6. The Bridgman growth of the succinonitrile–acetone alloy shown in Fig. 1 was modelled with the CA–FE model using a network of 175 × 175 square cells and triangular finite elements to impose the

Table 1. Growth kinetics and nucleation parameters

Succinonitrile–1.3wt% acetone alloy	
Growth kinetics: $v(\Delta T) = a_2 \cdot \Delta T^2 + a_3 \cdot \Delta T^3$	$a_2 = 8.26 \cdot 10^{-6}$ ms^{-1} K^{-2} $a_3 = 8.18 \cdot 10^{-5}$ ms^{-1} K^{-3}
Aluminium–7wt% silicon alloy	
Growth kinetics: $v(\Delta T) = a_2 \cdot \Delta T^2 + a_3 \cdot \Delta T^3$	$a_2 = 2.90 \cdot 10^{-6}$ ms^{-1} K^{-2} $a_3 = 1.49 \cdot 10^{-6}$ ms^{-1} K^{-3}
Nucleation law: $\frac{dn}{d(\Delta T)} = \frac{n_{max}}{\Delta T_\sigma \sqrt{2\pi}} e^{-[(\Delta T - \overline{\Delta T})/\sqrt{2}\Delta T_\sigma]^2}$	$\overline{\Delta T} = 5.5$ K $\Delta T_\sigma = 0.5$ K $n_{max} = 2 \cdot 10^{10}$ m^{-3}

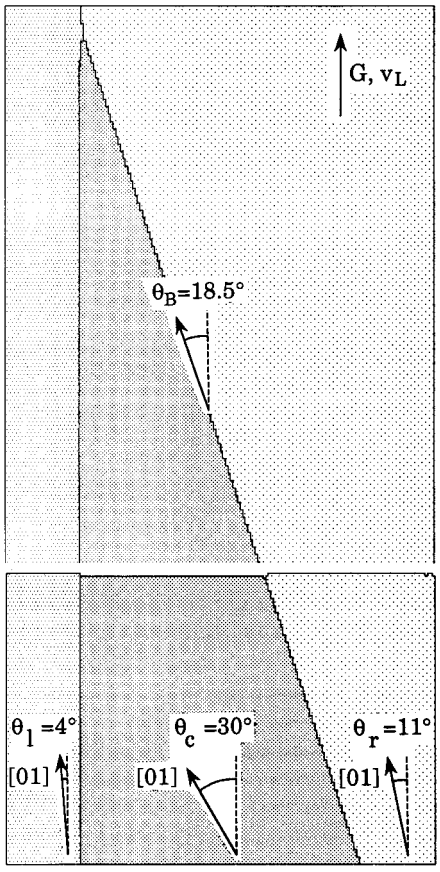

Fig. 6. Prediction of the grain growth and of the grain boundaries for the directional solidification of the organic alloy shown in Fig. 1 (cell density $n_c = 1782\,\text{mm}^{-2}$).

experimental thermal conditions ($G = 1900$ K/m, $v_L = 86 \cdot 10^{-6}$ m/s) [16]. For Fig. 6, the thermal gradient and the velocity of the liquidus isotherm were assumed to be given by the experimental arrangement. Therefore, the latent heat released by the grains was neglected in the computation and the only coupling was the temperature interpolation between the FE nodes and the CA cells. The growth kinetics of the dendrite tips was deduced from experimental measurements [16] (see Table 1). Three grains with crystallographic orientations corresponding to those seen in the experiment shown in Fig. 1 were nucleated in the bottom part of the domain before the start of the growth calculation. The orientations θ of the $\langle 10 \rangle$ directions for the left-hand (l), central (c) and right-hand (r) grains are indicated in Fig. 6.

As was already observed in the experiment shown in Fig. 1, the predicted interface of the central grain during growth (bottom part of Fig. 6) is at a lower temperature than that of the two external grains. The CA model is indeed able to reproduce the orientation dependence of the dendrite tip position. As a result, the calculated boundary between the converging left-hand and central grains is locked to a direction close to the left-hand grain orientation. On the other side of the central grain, the orientation θ_B of the predicted boundary between the two converging grains is in-between the orientations θ_c and θ_r of the two grains ($\theta_B = 18.5°$). This value is close to the experimental observation $\theta_B = 19°$. However, as shown in Fig. 7, the prediction of the grain boundary between the two diverging grains of Fig. 1 depends upon the density of cells, n_c, used in the CA network: when the cell density increases from 50 to 500 mm^{-2} (i.e. l varies from 141 to 45 μm), the orientation, θ_B, of the computed grain boundary increases from 12 to 18.5°. Above 500 mm^{-2}, it remains almost constant.

It is interesting to compare the CA cell size ($l = 45\,\mu$m) associated with the converged value of the grain boundary with the secondary dendrite arm spacing, λ_2. The value measured by Esaka close to the dendrite tips, $\lambda_2 = 8.4 \pm 0.3\,\mu$m [16], is smaller than the cell spacing l. However, Esaka showed that the branching mechanism of secondary and tertiary arms, which is responsible for the grain competition, only occurs with "active" branches (i.e. with branches which have escaped from the solute field of their neighbours by statistical fluctuations). These "active" branches are spaced by several λ_2 values. Thus, the growth algorithm built in the CA model appears to predict the correct boundary between two grains of diverging orientations when the cell size is of the order of the spacing separating the "active" branches. Further experimental work is required, however, to validate the 2d growth algorithm and to verify this conjecture under various growth conditions (thermal gradient, solidification rate, grains configuration, alloy concentration).

Columnar-to-equiaxed transition

The previous example shown in Fig. 6 illustrates the ability of the model to simulate the grain selection which operates during the growth of columnar grains. But it only validates the growth algorithm part of the model and the FE to CA coupling [i.e. the temperature interpolation shown as the LHS arrow in Fig. 3].

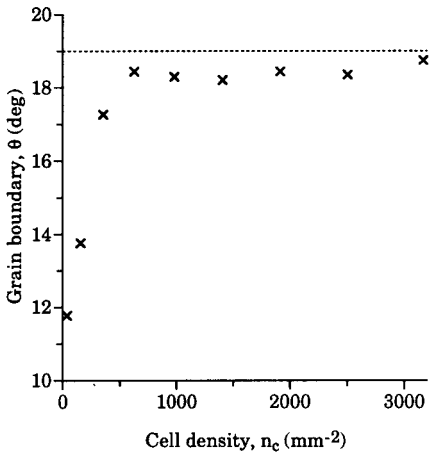

Fig. 7. Calculated angle of the boundary between the two diverging grains on the RHS of Fig. 6 as a function of the density of cells used in the CA calculation.

Table 2. Thermophysical properties of the Al–7wt% Si alloy (mainly Refs [31] and [41])

Thermal conductivity	κ	(W/m/°C)	175	at	$T=$ 10°C
			180		150°C
			150		577°C
			80		620°C
			90		650°C
			90		700°C
			110		750°C
Volumetric specific heat	ρc_p	(J/m^3/°C)	$2.44 \cdot 10^6$	at	$T=$ 27°C
			$2.65 \cdot 10^6$		227°C
			$2.84 \cdot 10^6$		427°C
			$3.50 \cdot 10^6$		660°C
Volumetric latent heat	ΔH_f	(J/m^3)	$9.50 \cdot 10^8$		
Melting point	T_m	(°C)	660		
Eutectic temperature	T_{eut}	(°C)	577		
Partition coefficient	k	(–)	0.117		
Slope of the liquidus line	m	(°C/%)	–6		

In order to test the fully coupled model (LHS and RHS arrows in Fig. 3), the CET presented in Fig. 2 has been simulated. The time-dependent boundary condition at the bottom of the Al–7wt% Si ingot was given by the heat flow calculated from the inverse method. The thermophysical properties of the alloy are listed in Table 2. A regular one-dimensional mesh of 100 elements was used to solve the implicit enthalpy formulation of the heat flow equation [equation (8)]. Since the thermal field was only one-dimensional, the interpolation coefficients, ϕ_{vn}, between the FE nodes and the CA cells were simply a function of the height. The heterogeneous nucleation at the bottom surface of the casting was assumed to occur near to the liquidus temperature with a very narrow Gaussian distribution. The parameters of the Gaussian distribution used to describe the heterogeneous nucleation in the bulk of the liquid were adjusted to match both the experimental cooling curves and the grain structure. These parameters are listed in Table 1 together with the growth kinetics of the dendrite tips of this alloy as calculated with the model of Kurz *et al.* [12].

The cooling curves and grain structure computed for the Al–7wt% Si ingot using the CA–FE model are presented in Figs 8 and 9, respectively. The calculated temperature evolutions of Fig. 8(a) correspond to the seven locations of the Pt–Pt10%Rh thermocouples shown in Fig. 2 and thus can be compared directly with the experimental cooling curves also shown in this figure. The excellent overall agreement of the calculated and measured curves seen in Fig. 8(a) is due to: (i) the well controlled one-dimensional heat extraction of the experimental arrangement; (ii) the precision of the temperature measurement in the copper chill and the associated inverse method used to deduce the boundary condition at the bottom of the ingot; (iii) the accuracy of the thermophysical properties of the alloy (see Table 2). (The vertical dotted line observed near 1650 s corresponds to the loss of thermocouple No. 7 after the ingot had solidified.) The formation of the interdendritic eutectic near 577°C which was simulated as an isothermal equilibrium reaction in the present model is clearly visible in the calculated cooling curves as small plateaux.

As for the deterministic micro-macroscopic approach of dendritic solidification [29], the deviations from equilibrium† predicted by the CA–FE model

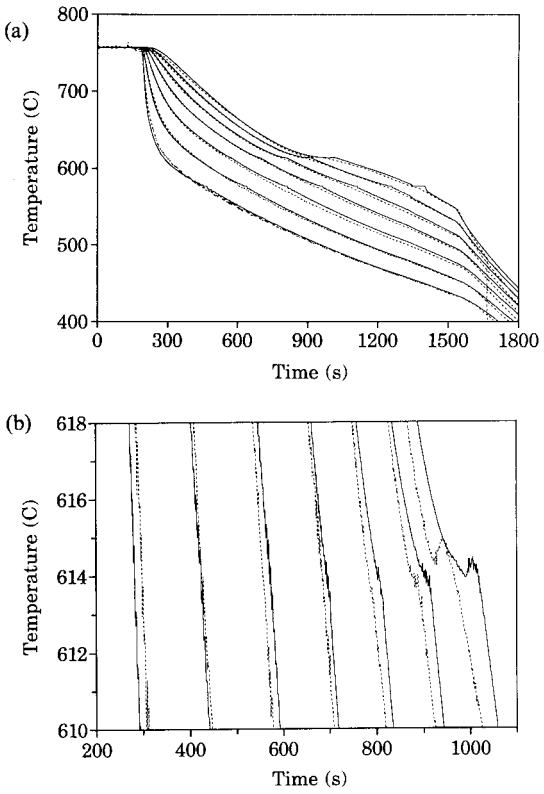

Fig. 8. (a) Experimental (dotted lines) and calculated (solid lines) cooling curves for the Al–7wt% Si alloy ingot shown in Fig. 2 (locations of the thermocouples: 20, 40, 60, 80, 100, 120 and 140 mm from the copper chill). (b) Magnification of the cooling curves shown in (a) near the liquidus temperature ($T_L = 618$°C).

†By the term "equilibrium" is meant all the models which assume complete mixing of solute in the liquid region (i.e. for which solidification starts at the liquidus temperature), even though back-diffusion in the solid already introduces non-equilibrium and non-reversible effects.

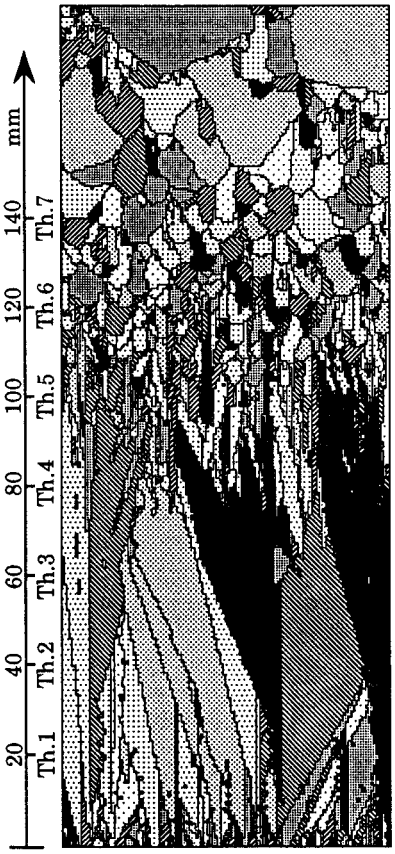

Fig. 9. Grain structure calculated with the CA–FE model for the longitudinal section of the Al–7wt% Si ingot shown in Fig. 2.

only occur in a small temperature region near the liquidus ($T_L = 618°C$). For this reason, Fig. 8(b) is an enlargement of Fig. 8(a) over an 8°C-temperature range below the liquidus. As can be observed, the simulated cooling curves exhibit some oscillations which are associated with the discrete nature of the cellular network. The amplitude of these oscillations is of the order of the measurement precision and of the noise of the measured cooling curves (± 0.2 K). More interesting are the slope variations of these curves at the various locations of the thermocouples. For the first three thermocouples nearest to the chill, the heat extraction is too large to permit the observation of any appreciable change in the slope of these curves below the liquidus. As the cooling rate decreases (in absolute value) with an increasing distance from the bottom surface, a change in the slope of the recorded cooling curves in the region of 614–615°C can be observed for the last four thermocouples. It should be noted that thermocouples Nos 4 and 5 are still located in the columnar zone (see Fig. 2) whereas the thermocouples Nos 6 and 7 are within the equiaxed region. Such variations in the slope of the cooling curves are associated with the beginning of solidification and are thus an indication of the local undercooling at which the microstructure forms. For columnar dendrites, this occurs at the time when the tips reach the corresponding thermocouple location and gives a direct estimation of the columnar undercooling [35]. Equiaxed grain morphologies are usually associated with the presence of a recalescence in the thermal history [29]. This is indeed the case for thermocouple No. 7 which is located in the equiaxed zone of the ingot (see Fig. 2) but is not the case for the previous thermocouples. This point is further discussed below.

As can be seen, the predictions of the CA–FE simulation are consistent with the measured thermal histories (occurrence of a slope change/recalescence in the cooling curve, temperature at which the change/recalescence occurs). The grain structure predicted by the model is shown in Fig. 9 and can be compared with the features of the experimental longitudinal micrograph of Fig. 2. At first glance, these microstructural features are well reproduced by the model. Among the many grains formed at the bottom surface of the ingot only a few long columnar grains succeed in growing. The grain competition which occurs among these grains is similar to the one presented previously for the succinonitrile–acetone alloy and a specific grain configuration. In this columnar zone, a few grains which have clearly nucleated in the bulk of the liquid ahead of the growing columnar front can also be seen (they are not connected with the bottom surface of the mould). Very often, these grains do not have a favourable orientation with respect to the vertical heat flow direction and they are therefore outgrown by the previously selected columnar grains. Accordingly, they appear as small "islands" in the columnar zone. If they have the proper orientation, however, they can grow and become elongated as was already observed for eutectic grains growing in a thermal gradient [15]. At about mid-height of the casting, the thermal gradient decreases and the undercooled liquid region ahead of the columnar dendrite tips becomes wider. Thus, the density of the grains nucleated in the bulk of the liquid increases and their growth finally stops the columnar front. These grains, however, still have an elongated shape because of the thermal gradient. As the thermal gradient continues to decrease in the remaining liquid, such grains finally become truly equiaxed in the upper part of the casting. In the experimental micrograph shown in Fig. 2, the presence of a few larger equiaxed grains can also be observed near the top surface of the ingot.

As already noted in Refs [36, 37], it is clear that the appearance of the columnar region in Fig. 9 is oversimplified when using a two- instead of a three-dimensional CA grain growth simulation. This is due to stereological effects associated with those grains which do not nucleate in the plane of the section micrograph but are intersected by that plane. The size of the truly equiaxed grains in the upper part of the simulated casting also differs from that of the experimental micrograph. Although stereological effects might also be invoked, the set of parameters chosen

for the Gaussian distribution (see Table 1) or the form of the nucleation law itself might be put in question. Nevertheless, many of the features seen in the micrograph of Fig. 2 are reproduced by the CA–FE model. In particular, it appears that the CET is not abrupt but occurs gradually: the long columnar grains are first blocked by elongated grains nucleated in the bulk of the liquid, these grains becoming more equiaxed as the gradient decreases. Providing the heat extraction and the gradient are small, a recalescence can be measured and predicted in the equiaxed region (thermocouple No. 7). The presence of stray grains (islands) formed by bulk heterogeneous nucleation in the bottom part as well as larger equiaxed grains near the top surface of the casting are also observed in both Figs 2 and 9.†

Considering the experimental and simulation evidence shown previously, it is difficult to give a unique and precise CET criterion for the one-dimensional Al–7wt% Si ingot (Figs 2 and 9). There is first a morphology transition at about 90 mm from the bottom of the casting (between thermocouples Nos 4 and 5) from the long columnar grains to elongated grains nucleated in the bulk of the liquid but growing in a thermal gradient. There is then another transition near the location of thermocouple No. 6 (120 mm) between elongated- and equiaxed-grain structures. Which of the two transitions corresponds to the CET? If the label "equiaxed grains" means "isotropic shape grains", then the CET occurs near the thermocouple No. 6 but if it corresponds to "grains nucleated in the bulk of the liquid", then the transition is below thermocouple No. 5. The same ambiguity arises if the definition of the CET is based upon the occurrence of a recalescence in the cooling curves. Although both thermocouples Nos 6 and 7 are located within the zone of grains nucleated in the bulk of the liquid, no recalescence is measured (and simulated) for the thermocouple No. 6. This can be explained by the fact that, at this location, the heat extraction through the bottom part of the casting (and thus the thermal gradient) is sufficient to remove the latent heat released by the equiaxed grains. In conclusion, there is a gradual change from long columnar grains (with a few isolated grains), to elongated grains and to finally equiaxed grains as the thermal gradient decreases.

Although it is difficult in these conditions to define clearly a CET criterion, the CA–FE model clearly reproduces the experimental microstructural features seen in Fig. 2 and the cooling curves shown in Fig. 8. In addition to directly producing a simulated micrograph, such an approach offers several advantages over the previously published deterministic models of solidification [29]. Firstly, it can treat in a single model both columnar and equiaxed microstructures. Secondly, it can account for the gradual change of the microstructure and for the CET. Thirdly, it can predict the shape of the grains nucleated in the bulk of the liquid whereas deterministic models always consider spherical envelops of the grains. Finally, it only predicts a recalescence when the thermal gradient is small whereas the micro-enthalpy scheme [31, 32] always gives a recalescence and the latent heat method [29, 38] produces undesired rebounding effects in the cooling curve. The present time-stepping scheme is similar to the micro-enthalpy scheme with a unique time step for both the heat flow and CA calculations but the main difference introduced by this technique is the spatial resolution used to calculate the microstructure development.

CONCLUSIONS

Although Zhu and Smith [5] have already published a coupling technique between a finite difference heat flow calculation and a Monte Carlo simulation of grain growth, the present contribution is the first fully coupled Finite Element–Cellular Automaton (CA–FE) model which includes the basic mechanisms of dendrite growth and serious comparisons with experimental data. At the microscopic scale of the CA cells network, the model is based upon a Gaussian distribution of the nucleation sites, the growth kinetics and the preferential growth directions of the dendrite tips. The resulting growth algorithm built in the CA model accounts for non-uniform temperature situations and is not biased by the cell network. For an organic analogue, it has been shown that this growth algorithm can produce the correct grain boundary between two converging and diverging grains providing the cell size is of the order of the spacing between "active" dendrite arms. On the macroscopic scale, the CA–FE model is based upon an implicit enthalpy formulation similar to the micro-enthalpy scheme used in deterministic micro–macro models of solidification [29, 31, 32]. The linear interpolation between nodes and cells allows the prediction of the capture and nucleation of cells in non-uniform temperature situations and to sum up the latent heat release at the FE nodes using a truncated Scheil approximation. The grain structure and the cooling curves calculated for a one-dimensional Al–7wt% Si ingot have been successfully compared with experimental results obtained under well-controlled conditions.

The applications of the CA–FE model presented here are not limited to castings. The main limitation of the model is due to the size of the dendritic grains

†Similarly to what has been demonstrated in Ref. [36], stereological effects might have been invoked to explain the formation of the stray grains (islands) seen in the columnar zone of Fig. 2 (i.e. columnar grains not nucleated in, but yet cut by, the plane of the cross section). However, in the present case, several observations make this explanation rather improbable: (i) the small size of these islands, (ii) the absence of these islands in the bottom part of the casting, (iii) the increased number of these islands with increasing distance from the copper chill (i.e. with decreasing thermal gradient).

which should not be too small with respect to the typical dimension of the process in order to limit the number of cells and the CPU time. The model has already been applied to the simulation of the dendritic network extension in a single crystal turbine blade near a re-entrant corner of the mould [39, 40]. Using such simulations, it is possible to calculate the undercooling at which the dendrite arms reach the end of the re-entrant corner as a function of the thermal gradient and isotherm velocity. This undercooling is important when assessing the danger of stray crystal formation at the head/foot of turbine blades. Interesting results have also been obtained with the present CA–FE model for the grain selection in investment castings, for the grain formation and CET in laser remelting, welding, continuous casting, strip casting, etc. Since stereological effects have a significant influence on the compound grain structures, the CA–FE model should be extended to three dimensions in order to achieve a successful comparison with experimental micrographs. Further developments in this direction are being made. Finally, the simple coupling technique proposed in the present contribution can certainly be improved to reduce the CPU time by using two steps for the FE and CA calculations.

Acknowledgements—The authors would like to thank the Commission pour l'Encouragement de la Recherche Scientifique, Bern, for providing a financial contribution to this research (Grant No. 2361.1) and the companies Sulzer-Innotec, Winterthur, and Calcom SA, Lausanne, for their contributions.

REFERENCES

1. S. G. R. Brown and J. A. Spittle, *Mater. Sci. Technol.* **5,** 362 (1989).
2. J. A. Spittle and S. G. R. Brown, *Acta metall.* **37,** 1803 (1989).
3. K. Ohsasa, private communication in *Modeling for Welding Science Workshop*, Florida (1993).
4. P. Zhu and W. Smith, *Acta metall.* **40,** 683 (1992).
5. P. Zhu and W. Smith, *Acta metall.* **40,** 3369 (1992).
6. Y. S. Yang, N. Black, T. B. Abbott and J. F. McCarthy, *Scripta metall. mater.* **29,** 1285 (1993).
7. M. P. Anderson, D. J. Srolovitz, G. S. Grest and P. S. Sahni, *Acta metall.* **32,** 783 (1984). See also by these authors: *Acta metall.* **32,** 793 (1984); *Acta metall.* **32,** 1429 (1984); *Acta metall.* **33,** 509 (1985); *Acta metall.* **33,** 2233 (1985).
8. Ph. Tavernier and J. A. Szpunar, *Acta metall.* **39,** 549 (1991).
9. A. D. Rollett, M. J. Luton and D. J. Srolovitz, *Acta metall.* **40,** 43 (1992).
10. L. Northcott, *J. Inst. Metals* **72,** 283 (1945).
11. B. Chalmers, *Principles of Solidification.* Wiley, New York (1964).
12. W. Kurz, B. Giovanola and R. Trivedi, *Acta metall.* **34,** 823 (1986).
13. M. Rappaz and Ch.-A. Gandin, *Acta metall.* **41,** 345 (1993).
14. Ch. Charbon and M. Rappaz, *Modelling Simul. Mater. Sci. Eng.* **1,** 455 (1993).
15. M. Rappaz, Ch. Charbon and R. Sasikumar, *Acta metall. mater.* **42,** 2365 (1994).
16. H. Esaka, Ph.D. thesis, No. 615, Ecole Polytechnique Fédérale de Lausanne, Switzerland (1986).
17. H. Esaka, W. Kurz and R. Trivedi, in *Solidification Processing* (edited by J. Beech and H. Jones), p. 198. Inst. Metals, London (1988).
18. W. Kurz and D. J. Fischer, *Fundamentals of Solidification.* Trans. Tech., Aedermannsdorf, Switzerland (1989).
19. R. N. Grugel and Y. Zhou, *Metall. Trans.* **20A,** 969 (1989).
20. J. Ampuero, Ch. Charbon, A. F. A. Hoadley and M. Rappaz, in *Materials Processing in the Computer Age* (edited by V. R. Volle *et al.*), p. 377. T.M.S., Warrendale, Pa (1991).
21. J. Ampuero, A. F. A. Hoadley and M. Rappaz, in *Modeling of Casting, Welding and Advanced Solidification Processes* (edited by M. Rappaz *et al.*), p. 449. T.M.S., Warrendale, Pa (1991).
22. Th. Imwinkelried and M. Rappaz, in *Euromat 91* (edited by T. W. Clyne and P. J. Withers), p. 191. Inst. Mater. London (1992).
23. W. C. Winegard and B. Chalmers, *Trans. Qt. Am. Soc. Metals* **46,** 1214 (1954).
24. B. Chalmers, *Aust. Inst. Metals* **8,** 255 (1963).
25. W. C. Johnston, G. R. Kotler, S. O'Hara, H. V. Ashcom and W. A. Tiller, *Trans. metall. Soc. A.I.M.E.* **233,** 1856 (1965).
26. K. A. Jackson, J. D. Hunt, D. R. Uhlmann and T. Seward III, *Trans. metall. Soc. A.I.M.E.* **236,** 149 (1966).
27. R. T. Southin, *Trans. metall. Soc. A.I.M.E.* **239,** 220 (1967).
28. J. D. Hunt, *Mater. Sci. Engng* **65,** 75 (1984).
29. M. Rappaz, *Int. Mater. Rev.* **34,** 93 (1989).
30. D. E. Ovsienko, G. A. Alfintsev and V. V. Maslov, *J. Cryst. Growth* **26,** 233 (1974).
31. Ph. Thévoz, Ph.D. thesis, No. 765, Ecole Polytechnique Fédérale de Lausanne, Switzerland (1988).
32. Ph. Thévoz, J.-L. Desbiolles and M. Rappaz, *Metall. Trans.* **20A,** 311 (1989).
33. S. C. Flood and J. D. Hunt, *J. Cryst. Growth* **82,** 543 (1987).
34. H. W. Hesselbarth and I. R. Göbel, *Acta metall.* **39,** 2135 (1991).
35. W. Kurz and R. N. Grugel, *Mater. Sci. Forum* **77,** 185 (1991).
36. Ch.-A. Gandin, M. Rappaz and R. Tintillier, *Metall. Trans.* **24A,** 467 (1993).
37. Ch.-A. Gandin, M. Rappaz and R. Tintillier, *Metall. Trans.* **25A** (1994).
38. C. S. Kanetkar, I. G. Chen, D. M. Stefanescu and N. El-Kaddah, *Trans. Iron Steel Inst. Japan* **28,** 860 (1988).
39. Th. Imwinkelried, J.-L. Desbiolles, Ch.-A. Gandin, M. Rappaz, S. Rossmann and Ph. Thévoz, in *Modeling of Casting, Welding and Advanced Solidification Processes* (edited by T. Piwonka *et al.*), p. 63. T.M.S., Warrendale, Pa (1993).
40. Th. Imwinkelried, Ph.D. thesis, No. 1120, Ecole Polytechnique Fédérale de Lausanne, Switzerland (1993).
41. R. D. Pehlke, A. Jeyrajan and H. Wada, *Summary of Thermal Properties for Casting Alloys and Mold Materials.* Univ. of Michigan (1982).